Desalination 417 (2017) 102–114

Contents lists available at ScienceDirect

Desalination

journal homepage: www.elsevier.com/locate/desal

Reverse osmosis membrane, seawater desalination with vibration assisted reduced inorganic fouling

Wende Li[a,*], Xu Su[a], Alan Palazzolo[a], Shehab Ahmed[b], Erwin Thomas[a]

[a] Department of Mechanical Engineering, Texas A & M University, College Station, TX 77840, United States
[b] Department of Electrical Engineering, Texas A & M University at Qatar, Doha, Qatar

ARTICLE INFO

Keywords:
Reverse osmosis
Inorganic fouling
Concentration polarization
Cross-flow velocity
Mass transfer coefficient

ABSTRACT

The subject of this work is the development of a novel vibration assisted seawater desalination approach which changes thermodynamic (mass transfer coefficient) and hydrodynamic (cross-flow velocity) properties to mitigate the inorganic fouling for RO membranes. A classical mass transport model and experimental measurements showed that an increased cross-flow velocity in the feed channel enhances the near membrane mass transfer coefficient, which promotes the back-diffusion of inorganic salts and reduces the concentration polarization (CP). Then a theoretical CP Finite Element Method (FEM) model incorporating increased cross-flow velocity reveals that a lower CP modulus forms near the membrane surface with a higher vibration frequency, which results in less fouling on the membrane surface. The vibration assisted desalination process was demonstrated using a linear motor driven, periodically oscillating desalination cell. A smaller flux decline was observed while using a higher vibration frequency (with a constant sinusoidal amplitude) and a higher vibration velocity (in multiple vibration forms). Process simulations and experimental observations validated that the proposed vibration assisted desalination process helps enhance the permeate flux and mitigate the formation of inorganic fouling on the RO membrane surface.

1. Introduction

Seawater desalination is a promising and important topic especially for coastal regions with a fresh water shortage. Seawater desalination processes can be broadly divided into two most commercially successful categories: membrane separation and thermal evaporation [1]. Among the various membrane separation technologies, Reverse Osmosis (RO) as a pressure driven membrane, has matured rapidly over the last few decades, and has become the choice of many projects for seawater or brackish water desalination and wastewater reclamation. RO has been recognized as the leading technology for desalination [2]. One of the main performance limitations in the pressure-driven membrane separation process is membrane fouling. Membrane fouling results from the deposition or accumulation of colloids and particles, organic macromolecules (organic fouling), sparingly soluble inorganic compounds (scaling), and microorganisms (biofouling) on the membranes surface [3] or into membrane pores such that membrane performance is deteriorated. Membrane fouling can cause severe product flux decline and reduce the quality of the product water. Usually feed pressure should be increased to keep a constant product flux, this causes elevated energy consumption. Also, severe membrane fouling may require intense physical/chemical cleaning or membrane replacement thus increases the operating costs of a treatment plant.

Hoek et al. proposed a comprehensive definition of RO membrane fouling, which is comprised of external fouling and internal fouling [4]. External fouling can be regarded as surface fouling (such as colloidal fouling, scaling, biofouling, etc.) while internal fouling is a change in membrane structure due to physical compaction or chemical degradation. Due to the complexity of the fouling formation process, sometimes the inorganic fouling caused by saturated inorganic particulates was classified into colloidal fouling (colloids of iron were usually studied with deposition or surface interaction methods) [3,5]. Sometimes inorganic fouling was treated as scaling (inorganic scale was usually studied with crystal nucleation and growth method) [6]. While in other cases the inorganic fouling was given a comprehensive view to study its forming mechanisms including deposition and crystallization regardless the definition of colloidal fouling or scaling [7]. This paper focused on an artificial seawater inorganic fouling and treated the inorganic fouling as a comprehensive formation process affected by multiple mechanisms, especially the concentration polarization phenomenon in the desalination process.

RO membrane fouling is a complicated problem affected by a

* Corresponding author.
E-mail address: liwende@tamu.edu (W. Li).

http://dx.doi.org/10.1016/j.desal.2017.05.016
Received 13 November 2016; Received in revised form 12 April 2017; Accepted 13 May 2017
Available online 20 May 2017

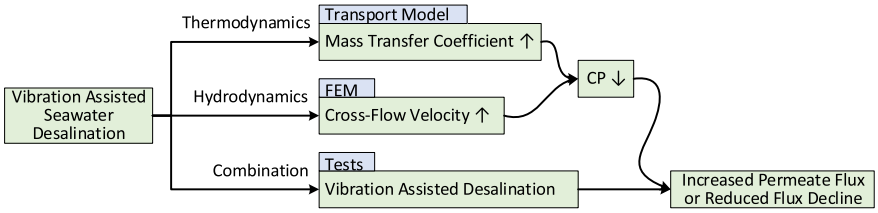

Fig. 1. Flowchart of the Vibration Assisted RO Desalination Study.

number of complex physical and chemical parameters. A. Fane et al. [3] summarized these factors into three categories: feed water characteristics, membrane properties, and hydrodynamic conditions. Membrane fouling is strongly affected by the hydrodynamics of operating conditions, such as filtrated flux and cross flow velocity. Thus, it is possible to improve the membrane filtration process by altering the hydrodynamic conditions at the membrane surface. In general, severe fouling can occur at higher membrane filtration flux and/or lower cross flow velocity. The cross-flow velocity is defined as the superficial velocity of the feed stream travelling parallel (tangential) to the membrane surface. The cross-flow velocity has a direct influence on the back-diffusion mass transfer coefficient during filtration. Gupta et al. [8] experimentally examined the enhancement of heat/mass transfer for a fluid undergoing pulsatile flow, which is consisting of sinusoidal pulsations superimposed on a steady laminar flow. Higher near membrane mass transfer coefficients promote the back-diffusion of inorganic salts and reduces the concentration polarization. Noticeably, concentration polarization plays a vital role in fouling formation in high pressure membrane systems, as it leads to elevated solute concentrations near the membrane surface. Concentration polarization arises due to the convection process driven by membrane filtration, as solvent may pass through the membrane, and rejected solute tends to accumulate in the vicinity of the membrane surface. A steady-state concentration gradient will be established when the solute convection process is balanced by the solute back-diffusion process. Elevated solute, especially inorganic ions, near the membrane surface may become supersaturated and increase the tendency of inorganic nucleation and further crystallization or scaling. A vicious circle arises due to cake-enhanced concentration polarization phenomenon [9], which is caused by the hindered back-diffusion of salt ions by deposited cake layers. T. Kennedy et al. [10] proposed that a high near wall velocity induced by pulsating flow helps counteract concentration polarization. Therefore, factors related to thermodynamics and hydrodynamics of operating conditions that enhance the back-diffusion process, such as higher cross flow velocity, will reduce the concentration polarization thus accordingly reduce inorganic membrane fouling.

Methods of altering the thermodynamics and hydrodynamics related to the operating conditions include: 1) changing the axial cross flow velocity and 2) changing the fluid-solid interface boundary layer, which can be realized by moving the membrane. In the cross-flow RO system, solely increasing the cross-flow velocity is usually achieved by increasing the operating pressures. However, both surface crystallization and bulk crystallization favor high operating pressures [6], thus this approach tends to promote the scaling of inorganic particles. Hadzismajlovic and Bertram [11] experimentally investigated a tubular ceramic MF unit with periodically interrupted cross-flow to enhance the flux of yeast suspension. The crossflow was interrupted periodically (6.3–6.8 Hz) by a pulsation generator. There was a maximum of 102% flux enhancement for the pulsating feed flow compare to steady feed flow. For RO desalination, however, much less experimental study as well as theoretical modeling is available about changing the filtration boundary's thermodynamics and hydrodynamics to enhance the membrane performance. One commercial application of the membrane moving approach to enhance the cross flow velocity in RO membrane filtration is the vibratory shear enhanced process (VSEP) features a torsional membrane motion [12]. The VSEP unit operates at a fixed frequency of approximately 55 Hz with an angular amplitude of 0° to 13°, corresponding to a linear motion of 0–3.2 cm at the outer edge of a 28-cm diameter disk. Experimental studies by S. Wei et al. of VSEP technique showed that an increased natural organic matter removal efficiency [13] and reduced inorganic scaling [14] were obtained. An increased shear rate γ was adopted by the same authors to explain the mechanism of VSPE effect [15]. The shear rate indicates a cross-flow velocity gradient, which is defined as $\gamma = velocity\ scale/length\ scale$ (s^{-1}). Larger cross-flow velocity induces higher shear rates causing an increased back-transport of particles away from the membrane surface, which results in a reduced concentration polarization. This effect is also termed shear-induced diffusion [16]. The rotational shaking method is limited by inconsistent shaking amplitude throughout the membrane area due to radial difference, thus might not fully utilize the vibration effects. Thorough theoretical modeling and simulation works to explain and improve this technology are also limited. Another approach associated with the hydrodynamics of operating conditions is the rotation of the RO module. Rotating RO takes advantage of high shear and the Taylor vortex instability to reduce the permeate flux decline related to concentration polarization and membrane fouling [17].

A novel vibration assisted desalination technique was developed in this study to address the RO membrane fouling problem arises from one of the major foulants, the inorganic salts, with the aim of increasing the permeate flux and enhancing the overall RO membrane performance. Fig. 1 shows that the overall studying approach for the vibration assisted desalination process. The thermodynamics was first studied including the modeling and measurements of mass transfer coefficient and concentration polarization in an enhanced shear rate condition based on a classical mass transport model. The hydrodynamics was then studied based on a developed finite element model for the concentration polarization profile simulation with cross-flow velocities added in the channel flow under different vibration conditions. The mathematical expressions listed in this paper for the thermodynamics transport model and the developed hydrodynamics FEM model were analytically or numerically solved using MATLAB. Finally, the vibration assisted desalination process was realized by a linear motor driven vibratory desalination cell. Both the normalized permeate flux and the modified fouling index were used in the experiments as membrane fouling metrics to evaluate the fouling mitigation effect for the proposed approach.

Simulation results and test observations showed that the vibration assisted desalination process facilitated the reduction of the concentration polarization through increasing the cross-flow velocity and enhancing the mass transfer coefficient at the filtration boundary. A reduced level of permeate flux decline indicated that there was less inorganic fouling on the membrane surface in the vibration assisted desalination compared to the traditional (non-vibrating) desalination process.

2. Materials and method

2.1. Membrane and chemicals

In this study, the flat sheet RO membranes were obtained from a commercial thin film composite polyamide RO assembly (spiral wound

Table 1
Formula for Artificial Seawater.

Reagent	Quantity (for 1 L distilled water)
NaCl	26.726 [g]
MgCl2	2.260 [g]
MgSO4	3.248 [g]
CaCl2	1.153 [g]

module) for seawater desalination (Hydranautics, SWC6). Each membrane sheet had an active membrane surface area of 60 cm^2 (3 cm × 20 cm, W × L) after installation. All membrane sheets were stored in distilled water in a 10 °C environment. The feed spacers and permeate carriers for the desalination cell were obtained from the same spiral wound module. The inorganic salts NaCl, $CaSO_4$, $MaCl_2$, and $MaSO_4$ were purchased from Fisher Scientific.

2.2. Feed solution composition

The feed solution was artificial seawater, with the calculated formulae shown in Table 1. The total dissolved solids (TDS) was about 32,000 ppm.

The artificial seawater solution was set standing about 24 h for full mixing. No extra pre-filtration was applied as pretreatment to the artificial seawater solution in order to promote membrane fouling in a relatively short period, and to exclude the influence of an extra filtration process on the quantity of inorganic salts.

2.3. Desalination cell apparatus

This study utilizes a desalination cell to investigate the vibration effect on the inorganic fouling at the RO membrane surface. As seen in Fig. 2, the desalination cell includes a top plate with a feed port and a retentate port; a bottom plate with two permeate ports; membrane elements including a feed spacer, a permeate carrier and a reverse osmosis membrane; and sealing elements including O-rings and rubber gaskets. High pressure artificial seawater from the pump goes into the feed port of the desalination cell. After the filtration process, product water flows out from the permeate ports, while concentrated water from retentate port can either flow into the feed tank to form a recycling system, or be collected for disposal.

The desalination cell was driven by a linear actuator (LinMot Inc., P01-48x360F/60x210) according to various signal trajectories with frequency and amplitude set by a driver unit (LinMot Inc., E1200-GP-UC). The mechanical system of the apparatus can be seen in Fig. 3, in which the cell was supported on two shafts and four linear bearings. Four springs connect the cell to ground, and are specified to achieve resonance in order to reduce the required energy consumption.

2.4. Flow-loop components

The flow loop of the test rig can be seen in Fig. 4. The test rig flow loop contains a feed tank, a diaphragm pump, and several transducers

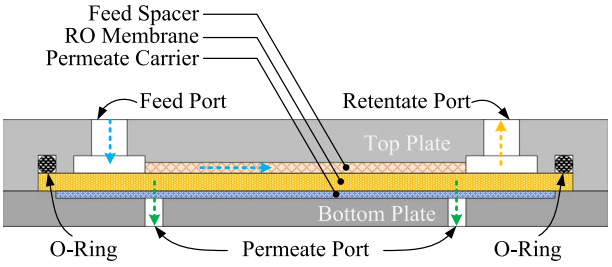

Fig. 2. Cross-Section Diagram of the Desalination Cell.

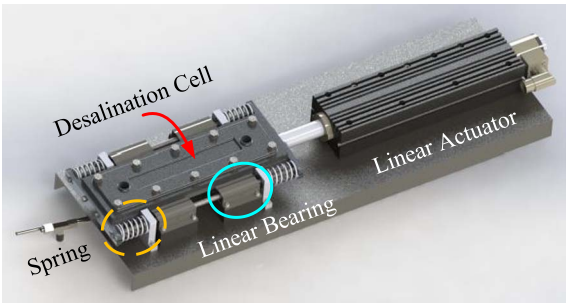

Fig. 3. Vibratory Desalination Cell Mechanical System.

for water pressure and flowrate measurement.

A diaphragm pump (Hydra-Cell, M03BABTHFECA) was used to provide high pressure (800 psi at 0.1 gpm) feed water to the desalination cell. A conductivity/salinity meter was used to measure the concentrations of feed, permeate and concentrate water. The conductivity meter has an EC accuracy of ± 0.01 μS/cm (Hana Instruments Inc., HI98192). A pressure relief valve was used to control the flow loop pressure (pressure can be monitored by pressure gauges), while a flow regulating valve was used to regulate the feed flow rate (flow rate can be monitored by flow meters). Finally, a pressure dampener was used to stabilize the feed pressure and eliminate the pressure fluctuation during the desalination process.

2.5. An enhanced mass transfer coefficient

The object of the thermodynamic and hydrodynamic analyses near the membrane surface during filtration process is to determine the concentration profile and the steady-state laminar fluid velocity profiles, as illustrated in Fig. 5. The fully developed axial velocity profile was modeled as Poiseuille channel flow, and the transverse/lateral velocity profile is modeled by porous membrane media near the membrane surface with boundary layer thickness δ_u. The axial velocity is assumed to be constant and the transverse velocity is assumed to be zero (channel flow without feed spacer) far from the membrane surface. Rejected solutes tend to accumulate near the membrane wall during the membrane filtration process, which is indicated in the concentration profile. This action forms a concentration boundary layer with thickness δ_C. The solute concentration is higher in this boundary layer than in the bulk flow. The concentration polarization of the solute ions accumulates and increases along the channel length (axial direction), thus permeate flux tends to decrease along the channel length as indicated by the permeate flux profile.

A portion of rejected ions near the membrane surface returns to the feed bulk as back-diffusion process, while other rejected ions accumulate near the membrane surface called the concentration polarization. The steady state concentration profile can be related to fluid statics [18] and is expressed in Eq. (1).

$$\frac{c_m - c_p}{c_b - c_p} = \exp\left(\frac{J_v \cdot \delta}{D}\right) = \exp\left(\frac{J_v}{k}\right) \tag{1}$$

in which c_m, c_p, c_b is the solute concentration near the membrane wall, at the permeate side, and at the feed side (bulk flow far from membrane wall), respectively. D is the solute diffusion coefficient (m^2/s), $k = D/\delta$ is the solute mass transfer coefficient, and J_v is the convective flux (volumetric flux, m/s) toward the membrane direction. Then the following Eqs. (2) and (3) were derived which establish a relation between observable concentration and the concentration near the membrane surface that would be difficult for direct observation:

$$\ln\left(\frac{1 - R_{obser}}{R_{obser}}\right) = \ln\left(\frac{1 - R}{R}\right) + \frac{J_v}{k}, \quad \begin{cases} \text{Define:} R_{obser} = \frac{c_b - c_p}{c_b} \\ \text{Define:} R = \frac{c_m - c_p}{c_m} \end{cases} \tag{2}$$

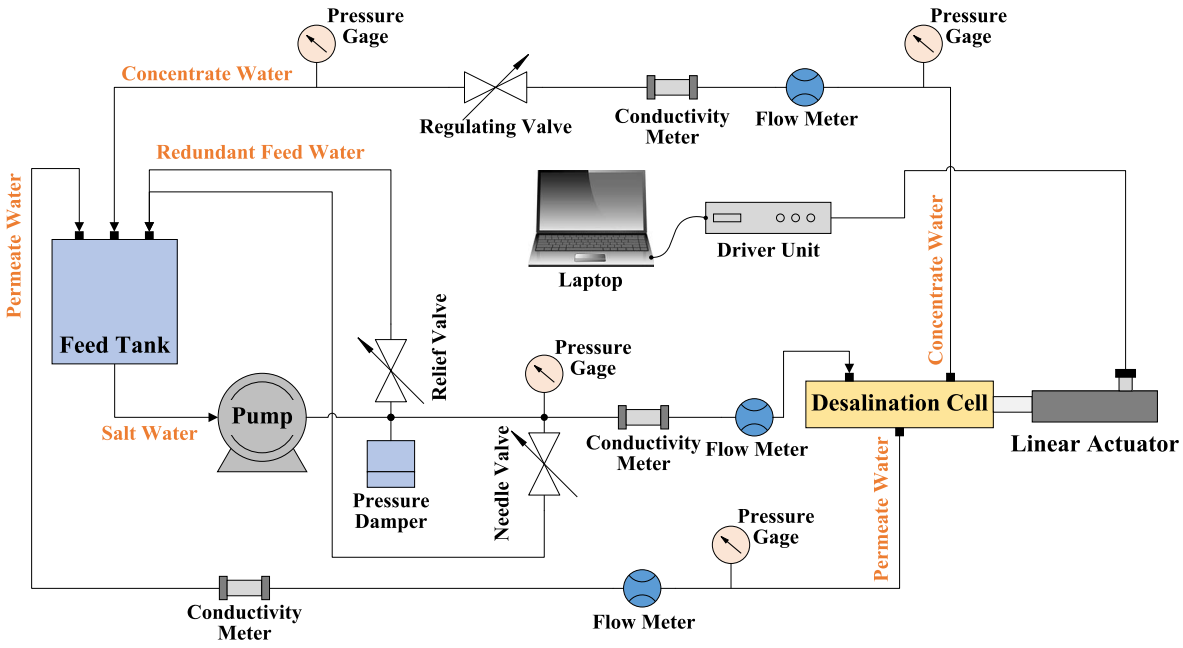

Fig. 4. Vibratory Desalination Cell Flow Loop System.

$$R = \frac{R_{obser}e^{J_v/k}}{1 - R_{obser} + R_{obser}e^{J_v/k}} \tag{3}$$

where R_{obser} is the observable removal efficiency using concentration of the bulk flow, and R is the true removal efficiency using concentration near the membrane wall. From the definitions of R and R_{obser}, the observable removal efficiency R_{obser} can be calculated since the bulk flow side concentration and the permeate side concentration can be measured by the conductivity meter. Then from Eq. (3) the true removal efficiency can be calculated based on the relation of R_{obser} and R. Further, based on obtained R and Eq. (2) the R definition, the concentration at the membrane surface c_m can thus be calculated, which will show the concentration polarization profile.

However, using Eq. (3) to calculate the true removal efficiency requires knowing the mass transfer coefficient k. For laminar flow in a thin rectangular channel, the mass transfer coefficient k can be related to the Sherwood number (Sh) through the following Eq. (4) [19].

$$\mathrm{Sh} = k\frac{d_h}{D} = 1.62\left(\mathrm{Re}\cdot\mathrm{Sc}\cdot\frac{d_h}{L_c}\right)^{1/3}, \begin{cases} \mathrm{Re}=\frac{ud_h}{\nu} \\ d_h = 2H_c \\ \mathrm{Sc} = \frac{\nu}{D} \end{cases} \tag{4}$$

where Re is the Reynolds number ($\mathrm{Re} = ud_h/\nu$, with u being the bulk crossflow velocity and ν the solution's kinematic viscosity, [m^2/s]), d_h is the channel's hydrodynamic diameter ($d_h \approx 2H_c$, with H_c being the channel height), Sc is the Schmidt number (ν/D), and L_c is the channel's length. There might be different relations between the Sherwood number and the mass transfer coefficient [20], but the basic form should be the same. Substituting the Re and Sc number into Eq. (4), yields the mass transfer coefficient

$$k = 1.62\left(\frac{uD^2}{2H_cL_c}\right)^{1/3} = 1.62\left(\frac{\gamma D^2}{12L_c}\right)^{1/3} \tag{5}$$

As defined in former section, γ is the shear rate (s^{-1}) at the membrane surface which represents the velocity gradient (du/dy) through a laminar hydrodynamic boundary layer. For a rectangular channel, the shear rate can be estimated based on its definition as

$$\gamma = \frac{6Q}{W_cH_c^2} = \frac{6u}{H_c} \tag{6}$$

in which Q is the feed flow rate, $u = Q/A$, $A = W_cH_c$ (channel cross-sectional area), and W_c is the channel width.

For turbulent flow, perhaps the best known heat-transfer correlation

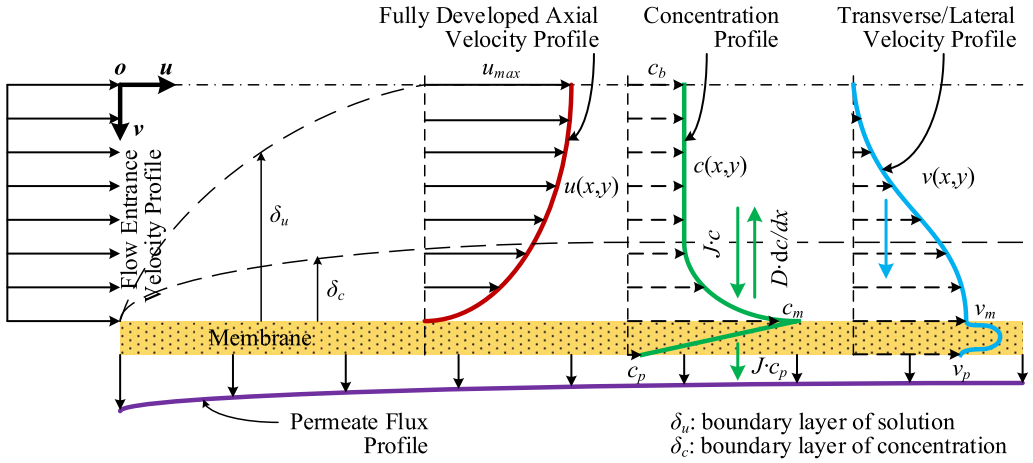

Fig. 5. Velocity and Concentration Polarization Profiles for Channel Flow.

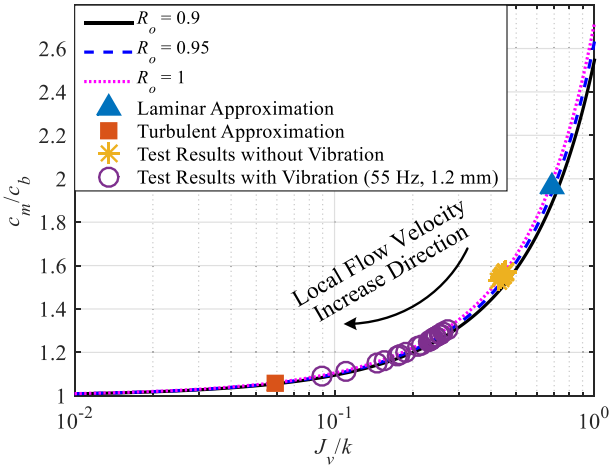

Fig. 6. Approximated and Measured Concentration Polarization Modulus.

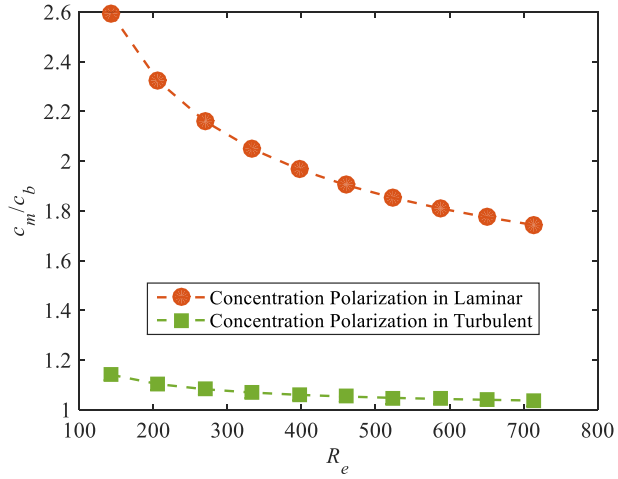

Fig. 7. Concentration Polarization Modulus vs. Reynolds Number.

for fully developed turbulence flow is from Dittus and Boelter, as [19,7]:

$$\mathrm{Sh} = 0.023\,\mathrm{Re}^{0.8}\,\mathrm{Sc}^{0.33} \tag{7}$$

Substitute Eq. (7) to Eq. (4) to obtain the mass transfer coefficient

$$k = 0.02\frac{u^{0.8}D^{0.67}}{H_c^{0.2}\nu^{0.47}} \tag{8}$$

The concentration polarization modulus which describes the concentration polarization phenomenon can be calculated using Eq. (2) as

$$\frac{c_m}{c_b} = (1 - R_{obser}) + R_{obser}\exp\left(\frac{J_v}{k}\right) \tag{9}$$

Fig. 6 is a plot of the concentration polarization modulus vs. J_v/k (known as Peclet number) under three observable removal efficiencies. It can be seen that the concentration polarization modulus increasingly deviates from unity (the origin of the coordinate) as the ratio J_v/k increases (as the flux through the membrane increases or as the mass transfer coefficient decreases). The laminar approximation of the concentration polarization modulus using mass transfer coefficient in Eq. (5) was also plotted in Fig. 6. The parameters used in this plot were based on the test conditions: bulk crossflow velocity $u = 0.2804$ m/s, convective flux $J_v = 1.5 \times 10^{-5}$ m/s, channel height $H_c = 0.75$ mm, channel length $L_c = 200$ mm, diffusion coefficient for NaCl $D = 1.61 \times 10^{-9}$ m^2/s, and observable removal efficiency $R_{obser} = 97\%$. Fig. 5 shows that the turbulent approximation of the concentration modulus based on the mass transfer coefficient in Eq. (8) is much lower than the laminar flow approximation due to larger local cross flow velocity in turbulence.

To measure the concentration polarization modulus data, the mass transfer coefficient was measured based on a simplified mass transfer coefficient measuring method [21]. First, high pressure pure water was used to feed the desalination cell and the permeate flux was measured. Then salt water of the same pressure was used and the permeate flux was measured. The mass transfer coefficient can thus be calculated as:

$$k = \frac{(J_v)_{\mathrm{salt}}}{\ln\left\{\frac{\Delta P}{\pi_b - \pi_p}\left[1 - \frac{(J_v)_{\mathrm{salt}}}{(J_v)_{\mathrm{pure}}}\right]\right\}} \tag{10}$$

In which ΔP is applied pressure, π_b-π_p is the transmembrane pressure, $(J_v)_{\mathrm{pure}}$ and $(J_v)_{\mathrm{salt}}$ are the permeate volume flux using pure water and salt water respectively. To eliminate the influence of temperature difference to Eq. (10) during the two tests, the permeate from pure feed water and temperature was fitted then the same temperature point was found as the saltwater's permeate. The concentration polarization with and without vibration can be calculated and also plotted Fig. 5 based on an experimentally measured mass transfer coefficient k. It is apparent that the measured concentration polarization is smaller than the laminar approximation, mainly due to the feed spacer (also called turbulent promoter) in the cell channel. However, the turbulent approximation of the concentration polarization is still lower than the real conditions, since the channel is too narrow for turbulence to fully develop [22]. Test data showed that after applying vibration to the desalination cell, the concentration polarization modulus can be reduced from 1.6 to about 1.2 (with fluctuations).

The reduction of the concentration polarization modulus can be explained with the changing of the cross-flow velocity (also the Reynolds number of the channel flow). Fig. 7 is an investigation result of the cross-flow velocity's influence on the concentration polarization modulus based on the lamina and turbulent mass transfer coefficient models. Result shows that with the increasing of the cross-flow velocity and the channel flow Reynolds number, the concentration polarization modulus can be reduced. While it should be noted that in actuality, the concentration polarization modulus will be located between the range of laminar approximation and turbulent approximation.

2.6. A reduced CP simulation based on a FEM model

The concentration polarization phenomenon was simulated using the finite element method (FEM) to model the vibration assisted desalination process. A concentration distribution of the feed solution in a membrane-plate channel (2-D) was obtained by solving a convection-diffusion equation which describes the physical phenomena involving the diffusion and convection of particles. The fluid velocity profiles required in the convection-diffusion equation, which can be expressed by numerical solutions, enable us to investigate the vibration effect on the concentration distribution in the feed channel.

2.6.1. Governing equations

The stationary convection-diffusion equation is [23,24]:

$$u\frac{\partial C}{\partial x} + v\frac{\partial C}{\partial y} - \frac{\partial}{\partial x}\left(D_{sx}\frac{\partial C}{\partial x}\right) - \frac{\partial}{\partial y}\left(D_{sy}\frac{\partial C}{\partial y}\right) - S_c = 0 \tag{11}$$

In Eq. (11), C is the variable of concentration for the mass transfer process, D_{sx} and D_{sy} are the diffusion coefficients in x and y direction in a 2-D Cartesian coordinate, u and v are the velocity profiles in the feed channel that the inorganic particles are moving with, and S_c describes the sources or sinks of the quantity C.

The diffusion may be approximated as isotropic for most numerical simulations [24], thus we assume a constant diffusion coefficient $D_{sx} = D_{sy} = D_s$. And since there is no sources or sinks in the channel ($S_c = 0$), the convection-diffusion equation to be solved (governing equation) by FEM becomes:

$$u\frac{\partial C}{\partial x} + v\frac{\partial C}{\partial y} - D_s\left(\frac{\partial^2 C}{\partial x^2} + \frac{\partial^2 C}{\partial y^2}\right) = 0 \tag{12}$$

The numerical solution of Eq. (12) based on the FEM requires the fluid velocity profiles of u and v for the feed solution in the channel. Berman [25] proposed a perturbation technique to solve the Navier-Stokes equation and obtain the steady-state velocity profiles for laminar flow within a porous channel, as seen in Eq. (13). Moussy and Snider [26] also used a similar technique for laminar flow over an array of porous pipes. These solutions give a good approximation in the case of small values of permeation velocity and channel height (or tube radius). The particle transport was assumed to have no effect on the velocity field.

$$\begin{cases} u(x,y) = \frac{3}{2}u_0\left[1 - \frac{v_w x}{u_o h}\right]\left[1 - (\frac{y}{h})^2\right]\left\{1 - \frac{v_w h}{420\eta}\left[2 - 7(\frac{y}{h})^2 - 7(\frac{y}{h})^4\right]\right\} \\ v(x,y) = \frac{1}{2}v_w\frac{y}{h}\left[3 - (\frac{y}{h})^2\right] - \frac{v_w^2 h}{280\eta}\left[2 - 3(\frac{y}{h})^2 + (\frac{y}{h})^6\right] \end{cases} \tag{13}$$

In Eq. (13), u_0 is the inlet velocity for the feed channel, v_w is the fluid transmembrane velocity, h is half the channel height, and η is the kinematic viscosity of seawater. The transmembrane velocity is given by [27] $v_w = P_{er}\cdot(\Delta P - \Delta\pi)$, with P_{er} the permeability constant of the RO membrane, ΔP the applied pressure, and $\Delta\pi$ the osmotic pressure between feed and permeate. It should be noted that these velocity profiles did not consider the feed spacers in the channel. There are in-depth discussions about the velocity profiles with feed spacers considered in a parallel plate channel [28,29] for reader's interest in the fluid flow behaviors in a complex geometric environment.

2.6.2. Finite element formulation

A finite element model FEM was developed to solve the governing convection-diffusion equation to obtain the concentration profile in the channel. A general treatment of the FEM can be found in [30], and detailed discussions of the FEM for convection-diffusion problems are presented in [31].

In finite elements, the solution of the differential equations is approximated by:

$$u(x) = \sum_{j=1}^{n} k_j \varphi_j(x) \tag{14}$$

This approximation is represented as a linear combination of unknown parameters k_j and known "shape:" functions φ_j of position x in the domain Ω. Thus, the solution of governing equation Eq. 12 is assumed to have the form

$$C(x,y) = \sum_{j=1}^{n_e} c_j^e \psi_j^e(x,y) \tag{15}$$

where c_j^e are the values of the concentration solution $C(x,y)$ at the nodes of a specific element e, and ψ_j^e are the shape functions over that element. The approximate solution C over a given element is completely known only when the node values c_j^e at every node of that element are known. Discretized algebraic equations to be used obtain the concentration at specific nodes c_j^e are:

$$\sum_{j=1}^{n} (K_{ij}^e + H_{ij}^e)c_j^e = Q_i^e \tag{16}$$

where matrix $[K_{ij}^e]$, $[H_{ij}^e]$ and vector $\{Q_i^e\}$ are:

$$K_{ij}^e = \frac{\beta_j u^e}{6} + \frac{\gamma_j v^e}{6} + D_s\left(\frac{\beta_i\beta_j}{4A_e} + \frac{\gamma_i\gamma_j}{4A_e}\right) \tag{17}$$

$$H_{ij}^e = -\left(\frac{v_{12n}h_{12}^e}{6}\begin{bmatrix}2&1&0\\1&2&0\\0&0&0\end{bmatrix} + \frac{v_{23n}h_{23}^e}{6}\begin{bmatrix}0&0&0\\0&2&1\\0&1&2\end{bmatrix} + \frac{v_{13n}h_{13}^e}{6}\begin{bmatrix}2&0&1\\0&0&0\\1&0&2\end{bmatrix}\right) \tag{18}$$

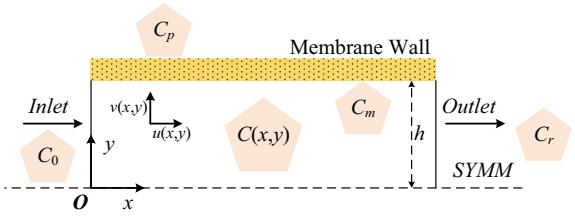

Fig. 8. Boundary and Domain of the Finite Element Solution.

$$Q_i^e = -\frac{1}{2}C_p\begin{pmatrix} v_{12n}h_{12}^e + v_{31n}h_{31}^e \\ v_{12n}h_{12}^e + v_{23n}h_{23}^e \\ v_{31n}h_{31}^e + v_{23n}h_{23}^e \end{pmatrix} \tag{19}$$

In the matrix $[K_{ij}^e]$, u^e and v^e are average velocities of the three nodes in an element (labeled e), β and γ are the coefficients of the interpolation function for the element e, and A_e is the area of the element e. In $[H_{ij}^e]$ and $\{Q_i^e\}$, v_{12n}, v_{23n}, v_{31n} are the velocity normal to the boundaries of the triangle element, while h^e is the length of an element boundary. Detailed derivations of the characteristic matrices and parameters are provided in the Appendix A.

2.6.3. Boundary conditions

The boundary conditions of the channel domain are illustrated in Fig. 8. Although in the test cell, the feed channel was composed of the RO membrane and the metal plate, a symmetry boundary was set at the middle of the channel based on the assumption that the vertical permeate flow is much smaller than the bulk flow in horizontal direction [24]. The feed concentration at the inlet of the channel was set to be a constant value C_0, while no specific boundary conditions were set at the outlet boundary. Other typical boundary conditions [32] were listed in Eq. (20).

$$\begin{cases} C(0,y) = C_0 \quad \text{(inlet)} \\ \frac{\partial C(x,0)}{\partial y} = 0 \quad \text{(symmetric boundary)} \\ D_s\frac{\partial C(x,h)}{\partial y} = v_n[C(x,h) - C_p] \quad \text{(permeable boundary)} \end{cases} \tag{20}$$

in which v_n is the velocity normal membrane wall.

As discussed, the contour integral in Eq. (17) only applied to the permeable boundary (at membrane wall), while at the symmetry boundary, a Neumann boundary condition is used since there is no fluid flow across the boundary ($q_n = 0$).

The finite element method FEM [30] assembles the element matrices Eqs. (17)–(19) to obtain a set of algebraic equations. The concentration field in the plate-membrane channel can be obtained by solving the algebraic Eq. (16) while including the boundary conditions expressed in Eq. (20).

The parameter values used in the numerical solution are summarized in Table 2.

In Table 2, the membrane permeability was determined from the

Table 2
Parameter Used in Finite Element Method.

Membrane characteristics	Definition
R' = 97%	Rejection rate
L = 200 [mm]	Membrane effective length
W = 30 [mm]	Membrane effective width
$P_{er} = 3.19 \times 10^{-12}$ [m/s·Pa]	Permeability constant*
Fluid properties	
$\eta = 1.05 \times 10^{-6}$ [m²/s]	Kinematic viscosity of seawater
C_0 = 32,000 [mg/L]	Inlet concentration
$D_{sw} = 1.61 \times 10^{-5}$ [cm²/s]	Diffusion coefficient [27]

* Permeability constant, or water permeability through the membrane, defined as the permeate flux induced by unit applied trans-membrane pressure. Note, the permeability unit should be [m/s/Pa] or [m/(s·Pa)].

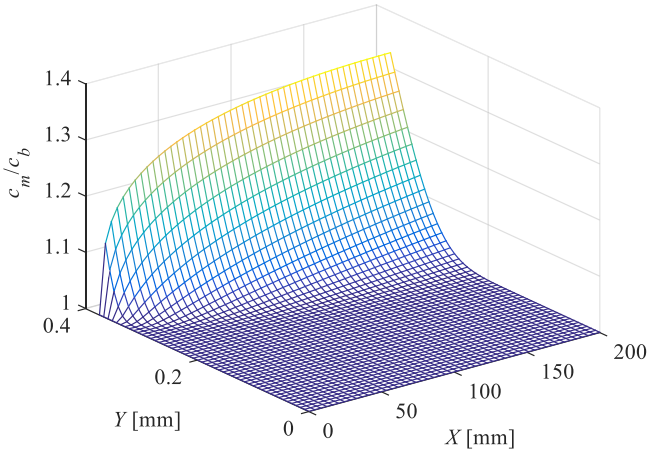

Fig. 9. Concentration Profile in Membrane Channel.

membrane resistance and dynamic viscosity of seawater ($P_{er} = 1/(\mu R_{os})$, $\mu = 0.00096$ N·s/m^2, $R_m = 3.26 \times 10^{14}$ m^{-1}), and the membrane resistance was measured before the test using the method introduced by E. Hoek [9].

The finite element code generates the mesh, computes the element matrices and total model matrix, imposes the boundary conditions and solves the algebraic equations. The FEM solution provides the concentration data at all nodes on the mesh, including the concentration of salts at the membrane surface C_m. The permeate flux was expressed as $v_w = P_{er}(\Delta P - \Delta\pi)$ (in which ΔP is applied pressure and $\Delta\pi$ is the osmosis pressure). Thus, the osmosis pressure varies with the forming of concentration polarization at the membrane wall, and the permeate flux v_w will change accordingly. For the first iteration of the program, v_w was calculated assuming no concentration polarization, and was updated after every iteration when the wall concentration was obtained until convergence was reached. The calculated salt concentration at each node was plotted as the concentration profile in Fig. 9. The X axis is the channel length direction, and the Y axis is the channel height direction. The membrane surface is located at $Y = 0.375$ mm, where the concentration polarization is formed.

Fig. 9 shows that the concentration polarization modulus near the membrane surface increases along the membrane channel length direction (X axis), corresponding to experimental observations [33], in which optical images of the scaled membranes revealed that gypsum scale coverage increased toward the channel exit. At the channel outlet, the CP modulus is about 1.33.

Shaking of the RO membrane in the vibration assisted desalination process creates a relative velocity between the RO membrane surface and the inertial fluid flow. Reference [10] proposed a theoretical analysis for a process of applying a pulsed flow to a membrane-lined reverse osmosis tube to increase the permeate flux, in which the oscillating component of velocity was directly imposed on the flow through the pipe. Similarly, for the vibration assisted desalination analysis based on the FEM, the root mean square (RMS) value of the relative velocity was added to the cross-flow velocity profile along the channel length direction (also the shaking direction), while the vibrating effect in the channel height direction was ignored. The peak-to-peak amplitude of the vibration was approximately 1.2 mm with frequencies ranging from 0 Hz to 55 Hz. Concentration polarization moduli at the membrane surface under different vibration conditions were extracted from the concentration profile and were plotted in Fig. 10.

Fig. 10 shows that the concentration polarization moduli in the vibration assisted desalination process were lower than the without vibration case from the inlet (upstream) to the outlet (downstream) locations. This suggests that the vibration retarded the formation of concentration polarization upstream of the channel length, and then the vibration reduced the concentration accumulation downstream of the

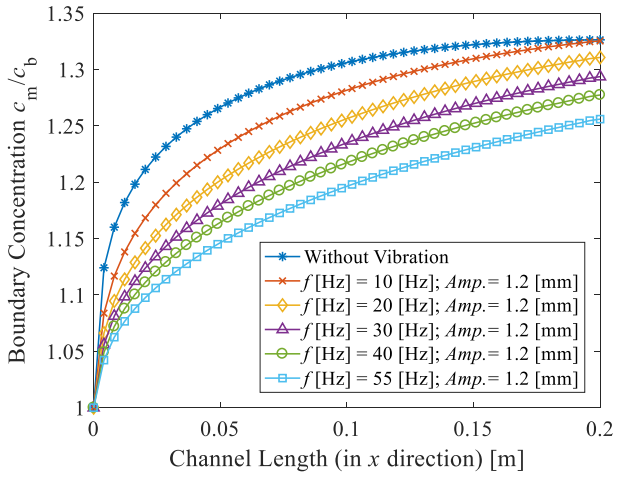

Fig. 10. Concentration Polarization Modulus under Different Vibrating Conditions.

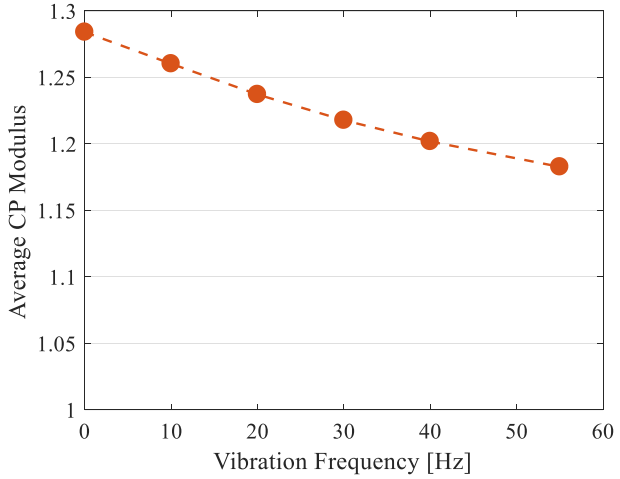

Fig. 11. Average Concentration Polarization Modulus of the Channel.

feed channel. To better illustrate the relation between vibration frequency and the concentration polarization modulus, the average value of CP modulus of the whole channel was calculated by Eq. (21) and plotted in Fig. 11.

$$c_{ave} = \frac{1}{x_b - x_a}\int_a^b c(x)dx \tag{21}$$

In Eq. (21), $c(x) = c_m/c_b$ is the boundary concentration along the channel length direction. Also, $a = 0$ is the lower limit of integral at the beginning position of the channel, and $b = 0.2$ m is the upper limit of integral at the end position of the desalination channel.

Fig. 11 shows that the CP modulus was reduced gradually from 1.284 in the no-vibration case to 1.183 in the 55 Hz vibration case. Fig. 12 shows the predicted permeate velocity for the entire channel vs. vibration frequency. Averaging the permeate velocity by integrating along the cell channel length one finds that there is a 10% permeate velocity increase from 7.85×10^{-6} m/s without vibration to 8.62×10^{-6} m/s with 55 Hz 1.2 mm vibration. Higher frequency shaking with a millimeter scale vibration amplitude is not only energy consuming but also difficult to realize with readily available electro-mechanical driving methods. Thus, the vibration frequency in the test rig was set in the range of 20–60 Hz.

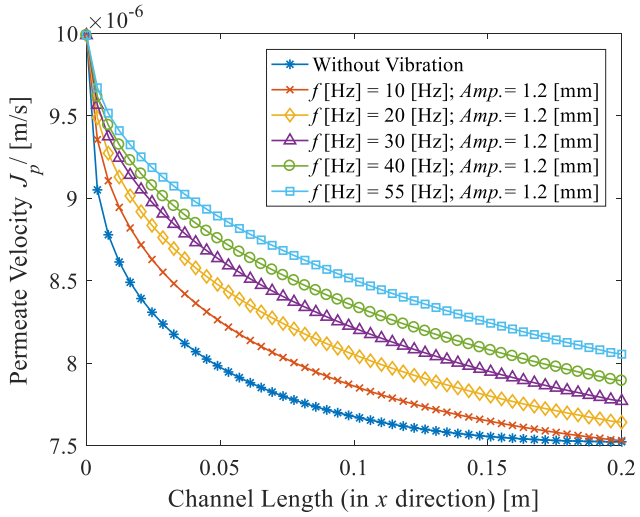

Fig. 12. Average Permeate Velocity of the Channel.

3. Test results and discussion

3.1. Metrics of membrane fouling

To understand the factors that govern membrane fouling and develop mitigation strategies, many studies have compared different processes, coatings, etc. using flux decline as a metric [34,35]. Flux decline (the change in flux due to fouling divided by the initial flux) quantifies the effect of fouling on the productivity of a given process, but does not give an insight into the accumulation of foulant itself [36]. The two commonly used fouling indices in the industry are silt density index (SDI) and modified fouling index (MFI) [37] (the MFI is an extension of the SDI).

The Modified Fouling Index is a very useful method for explaining and predicting the rate at which fouling of reverse osmosis membranes occurs [38]. The MFI fouling metric was derived by Schippers et al. based on the well-known cake filtration equation for RO membrane filtration, and the cake filtration equation is one of the well accepted and mature theories to explain the inorganic scaling or surface crystallization [7]. Thus, the MFI is a good method to characterize the inorganic fouling formation during desalination test both with and without vibration. The MFI method was used but not directly mentioned in some publications. For example in [39], filtration data of different feed compositions was compared and membrane resistance was estimated by a cake filtration theory, which is exactly the same as MFI method. Although the MFI method was developed for dead-end filtration, its fouling interpretation idea can be applied in a cross-flow mode [40,37,39] since filtration by a membrane is the common working mechanism for both modes and only feed conditions differs. The level of fouling on the RO membrane surface can be obtained by comparing the MFI values for the with/without vibration cases under the same operating conditions (such as applied transmembrane pressure, membrane characteristics etc.)

In this study, both permeate flux decline and the modified fouling index (MFI) were selected as membrane fouling metrics during the tests.

3.2. Experimental procedures

The vibration assisted desalination process was demonstrated utilizing a desalination cell driven by a linear motor. The experimental setup and feed solutions were discussed in the Materials and method section. There were no pre-filtration or other pretreatment applied to the artificial seawater, so the observed time for fouling formation in the experiments were correspondingly reduced. To disassociate any flux declines due to the compaction of the membrane, the membrane was compacted using distilled water until the filtration flux was stable before fouling tests were performed [36]. As a result, any flux decline measured during the tests was assumed to have been caused by surface fouling only.

The membrane sheet was replaced with a new one after each set of tests. A typical experimental run covered a time period of 7 to 8 h. The permeate volume was collected in a graduated cylinder at intervals of 5 to 10 min and was weighed on a digital balance. The permeate water was returned to the feed tank after measuring to maintain the feed concentration constant. A volume to flux conversion was made by dividing the collected volume by the time period, and a conversion to permeate velocity was made by dividing the permeate flux by the active area of the membrane sheet. Water temperature is one of the key factors in the performance of reverse osmosis membranes. RO membrane productivity is very sensitive to changes in the feedwater temperature, and as the water temperature increases the permeate flux increases almost linearly, due primarily to the higher diffusion rate of water through the membrane. Permeate flux was corrected according to the temperature correction factors (TCF) for polyamide membrane to eliminate the effect of temperature fluctuations of the feed water during controlled group tests due to the limited temperature control facilities. Membrane manufacturers provide temperature correction factors for given operating temperatures and can vary by manufacturers. For polyamide RO membrane, an empirical formula Eq. (22) was given by the membrane manufacturer (Hydranautics Corp.),

$$TCF = e^{k_t\left(\left(\frac{1}{298}\right)-\left(\frac{1}{273+t}\right)\right)} \tag{22}$$

where TCF is temperature correction factor, k is a constant characteristic for a given membrane material, and t is feed water temperature in degrees Celsius. In this equation, a temperature of 25 °C is used as a reference point, with $TCF = 1$. The membrane coefficient of $k_t = 2700$ was used [41] based on data collected from an water treatment plant. Tests were performed to determine a suitable temperature correction factor for the current desalination cell test rig. It was found that the TCF was different for pure water and salt water. Salt solution of 32,000 ppm NaCl was used but no other chemicals were added to eliminate membrane fouling during the test. The membrane was compacted before the test and only the temperature varied during the test (from 25 °C to 45 °C). One membrane sheet was used for two successive tests but a pure water flush was applied between the two tests to clean the membrane. The temperature correction factor from a public database (interested readers may find the database from several sources, such as public reports from water treatment plants), from the empirical formula and from tests were plotted in Fig. 13.

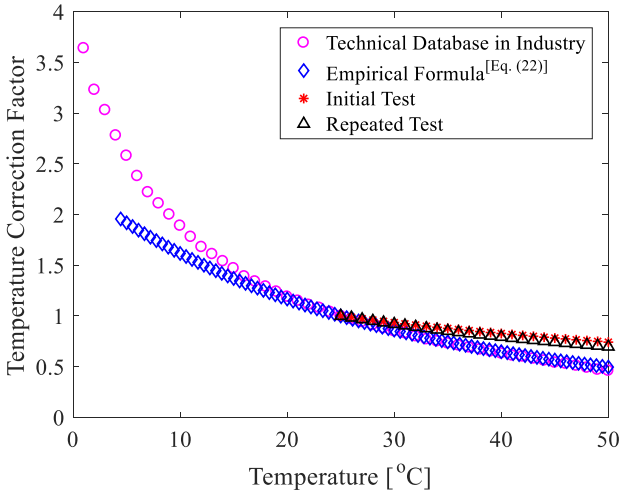

Fig. 13. Temperature Correction Factor from Database, Calculation and Test.

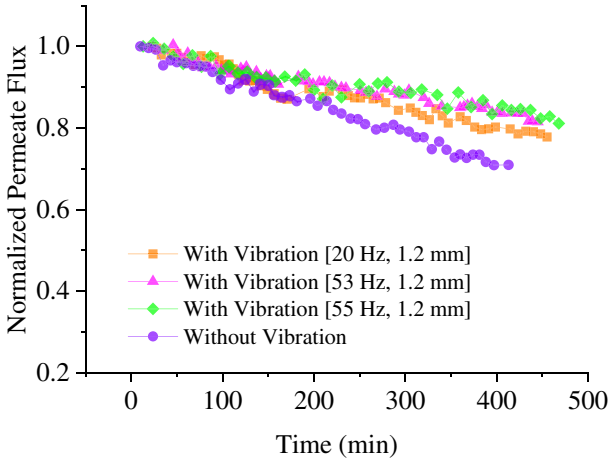

Fig. 14. Permeate Flux under Different Test Conditions.

Measured permeate flux was corrected by the tested temperature correction factor. Fig. 14 shows the temperature corrected permeate flux under different vibration conditions. The permeate flux declined in all three control groups during the approximately 400 minute tests. The permeate flux declined 29% without vibration, 20% with vibration at 20 Hz, and16% and 15% with vibration at 53 Hz and 55 Hz, respectively. The MFI method results will be shown to more clearly distinguish between the 53 Hz and 55 Hz cases.

3.3. Modified fouling index values

As Schippers et al. proposed the following mechanisms may be involved in a membrane filtration process: the blocking filtration, the cake filtration without compression and the cake filtration with compression, as shown in Fig. 15 [42]. For RO membranes, which have no pores in general, cake formation need not be preceded by pore blocking fouling mechanisms [37]. Thus cake filtration and electrostatic interaction between impurities and the RO membrane surface are the main fouling mechanisms. So, there may be no blocking filtration observed during typical tests.

For the filtration process with cake fouling, the following Eq. (23) can be applied to the filtration rate [38]:

$$\frac{dV}{dt} = \frac{1}{\mu}\frac{\Delta P \cdot A_m}{(R_m + R_k)} \tag{23}$$

where ΔP is applied transmembrane pressure, R_m is the clean membrane resistance (m^{-1}), R_k is the resistance of the cake or gel per unit of area, A_m is the membrane area, V is the accumulated filtrate volume (m^3), and μ is the solution dynamic viscosity (Pa-*sec*). If there is no compression of the cake, then $R_k = I \times V/A_m$, in which I is the fouling potential index (m^{-2}). Integration while assuming constant ΔP yields

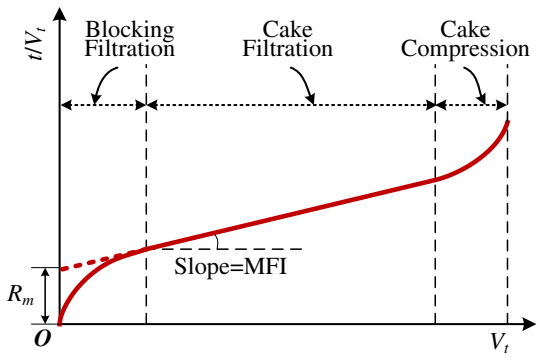

Fig. 15. Illustration of Modified Fouling Index during Filtration Process.

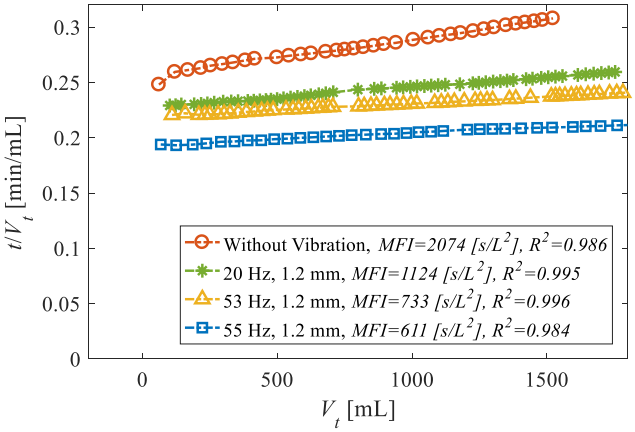

Fig. 16. MFI Values for RO Membrane under Different Test Conditions.

$$\frac{t}{V} = \frac{\mu R_m}{\Delta P \cdot A_m} + \underbrace{\frac{\mu I}{2\Delta P \cdot A_m^2}}_{MFI} V \tag{24}$$

The *MFI* value can be derived from the slope in the relation t/V versus V under specific operating conditions. If the *MFI* method is applied to an RO membrane desalination process, the permeate flux decline can be expressed as the change in the slope of Eq. (24), so the term *MFI* serves as an index for the membrane fouling tendency. The level of fouling on the RO membrane can be obtained by comparing the *MFI* slopes under the same operating conditions (such as applied transmembrane pressure, membrane characteristics etc.), and a higher *MFI* value means more fouling occurs on the membrane surface due to larger declining of the permeate flux (t/V is the reciprocal of permeate flux) [40]. As discussed by E. Brauns in [43], the linear relation between t/V and V with its slope being defined as the *MFI* value will only hold if the assumption of a simple linear relation between cake resistance and permeate volume according to $R_k = I \times V/A_m$ is valid. The MFI value results shown in Fig. 16 from the test data shown in Fig. 14 validates the assumption with a high linear correlation R-Squared values at least 0.98. Fig. 16 also shows that higher vibration frequencies corresponding to lower MFI values, indicating less membrane surface fouling based on the above discussions.

Slopes of the linear section of the curves in Fig. 16 provides information on the membrane surface fouling based on the cake filtration theory, while the absolute values of the curves reflect the absolute values of measured permeate flux which usually differs in different control groups due to concentration variance of feed solutions. Thus, the slops of the linear section of the curves provide more valuable information than the absolute values of the curves.

3.4. A correlation between vibration velocity and permeate flux

During vibration, the forced vibration velocity is directly applied to the desalination cell metal plate and the membrane sheet, disturbing the concentration polarization boundary layer and promoting the back diffusion of inorganic salts. Thus, it is interesting to study the correlation between vibration velocity and permeate flux besides the qualitative observations of reduced permeate flux declines under different vibration conditions. Fouling control publications quite often use normalized permeate flux to express the fouling control effect, an example being the examining of antiscalant effects in [33]. The normalized flux is defined as the value of the permeate flux divided by the initial flux J/J_0 (initial permeate flux was around 1.5×10^{-5} m/s). Here the normalized flux was also used but with a slightly different form, an averaged flux, which was obtained by time integration of the flux (about 450 min) to better distinguish the differences between each group of data, as seen in Eq. (25)

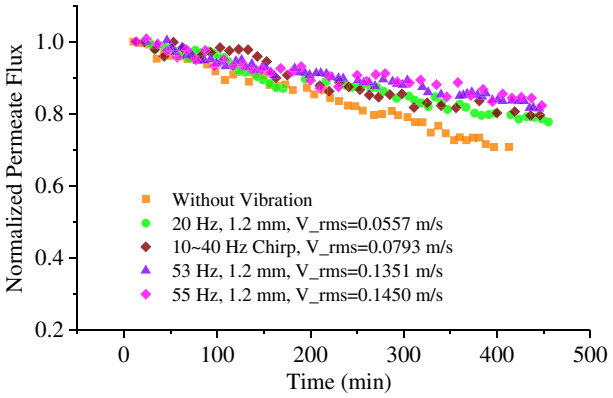

Fig. 17. Normalized Flux Under Different Test Conditions.

$$F_{Nave} = \frac{1}{t_b - t_a}\int_{t_a}^{t_b} F_N(t)\,dt \tag{25}$$

in which $F_N(t)$ is the time varying normalized flux and F_{Nave} is the time averaged normalized permeate flux.

The relation between vibration velocity and flux was studied based on a group of tests results with different vibration frequencies as shown in Fig. 14, and an extra test with a 10–40 Hz chirp signal. The selection of various forms of vibrations was intended to determine whether a relationship still exists between flux and vibration velocity under different forms of vibration. Although vibrations differed in forms, the calculated velocities (root mean square values used due to velocities alternating in direction) were gradually increasing, as shown in Fig. 17.

Fig. 18 is a plot of the relationship between the vibration velocity and the time averaged normalized permeate flux. Increasing the vibration velocity causes an increased normalized flux over the 450-minute test duration, and yields a lowered flux decline during the filtration periods. Finally, a correlation between the vibration velocity and the time averaged normalized flux was found by a linear fitting of the test data, as seen in Eq. (26).

$$F_{Nave} = 0.3202 \cdot V_{RMS} + 0.8268 \tag{26}$$

This correlation may be used as an initial permeate flux prediction in further applications of this technique when limited to vibration velocities (root mean square) less than 0.15 m/s and operation of an initial 8 h.

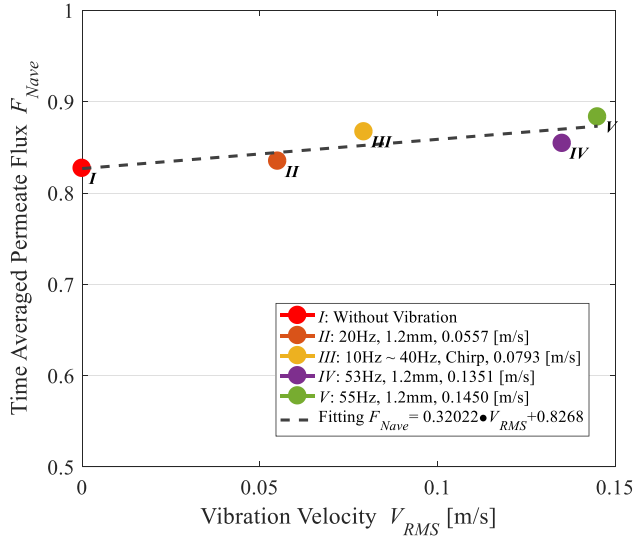

Fig. 18. Relation of Vibration Velocity and Permeate Flux.

4. Conclusions

Reverse osmosis membranes have been recognized as the leading technology for the desalination process, but their operation performance is limited by membrane fouling over long periods of time. Common fouling mitigating techniques involve feed water pretreatment, RO membrane coating and alteration of operating conditions.

This study focused on a vibration assisted desalination process based on the idea of changing the hydrodynamics of the operating conditions, especially increasing the local cross flow velocity. An enhanced mass transfer coefficient and a promoted back-diffusion process indicate that the vibration assisted desalination process also affects the thermodynamics of the operating conditions. The mechanism revealed by simulation results and test observations validated that the proposed fouling mitigation technique facilitated reducing the concentration polarization in a cross flow filtration process. There were flux declines in both the vibration and the without vibration cases. However, for the vibration assisted desalination process, the flux decline was slower than the case without vibration. After about 7 h of operation, the permeate flux declined 29% without vibration, 20% with 20 Hz vibration, 16% with 53 Hz vibration, and 15% with 55 Hz vibration (all with 1.2 mm vibration amplitude). Selected membrane fouling metrics indicated that less fouling formed on the membrane surface under these vibration conditions. Also, correlation between the permeate flux and the vibration velocity was established based on test data.

The inevitable power consumption for the vibration assisted desalination process is about 683 W for the 55 Hz 1.2 mm vibration by the linear actuator. While for 20 Hz 1.2 mm vibration the power consumption was only about 192 W and the effectiveness in raising the permeate flow was still very significant. It is to be noted that much larger membranes could be vibrated with small increases in power consumption due to the relatively light mass of the membrane.

Further studies may involve more accurate process simulation by considering the effect of foulant-foulant or foulant-membrane interactions in the vibration assisted desalination process, or experimental investigations of this technique to mitigate other types of fouling, such as colloidal fouling and organic fouling.

Nomenclature

c_m	concentration of salt at the membrane surface, [g/L] or [kg/m^3]
c_p	concentrate of salt in the permeate, [g/L] or [kg/m^3]
c_b	concentration of salt in the feed bulk flow, [g/L] or [kg/m^3]
D	diffusion coefficient (diffusivity), [m^2/s]
k	mass transfer coefficient, [m/s]
R	true removal efficiency
R_{obser}	observable removal efficiency
ν	kinematic viscosity, [m^2/s]
u	cross-flow velocity, [m/s]
L_c, W_c, H_c	channel length, channel width, and channel height, [m]
L, W	membrane effective length, membrane effective width, [m]
d_h	hydrodynamic diameter, $d_h \approx 2H_c$, [m]
Re	Reynolds number, Re = ud_h/ν
Sc	Schmidt number Sc = ν/D
ΔP	applied transmembrane pressure, [Pa]
γ	shear rate, [s^{-1}]
J_v	convective flux (volumetric flux), [m/s]
v_w	transmembrane velocity, [m/s]
P_{er}	Permeability constant, [m/(s·Pa)]
μ	dynamic viscosity, [N·s/m^2]
R_m	membrane resistance, [m^{-1}]
R_k	cake or gel resistance, [m^{-1}]
F_{Nave}	time averaged normalized permeate flux, [m/s]
TCF	temperature correction factor
MFI	modified fouling index

Acknowledgement

The authors of the paper would like to acknowledge the financial support from the Qatar National Research Fund (NPRP No.: 6-213-2-090, Centrifugal Pressure Vibrating Membrane Reverse Osmosis Desalination and Fracking Waste Water Recovery).

Appendix A. Finite element formulation

This section presents the detailed derivation of the developed finite element scheme to solve the governing convection-diffusion equation and to obtain the channel concentration profile as was presented in the paper. The derivation aims to obtain a group of discretized algebraic equations as seen in Eq. (A.10) to solve for concentrations c_j^e on all nodes and elements. Following the standard steps of the FEM weighted residual approach multiply the governing differential equation Eq. (12) with a weight function w and integrate the governing equation over a typical element. Trade differentiation from C to w using integration by parts [27], as seen in Eq. (A.1).

$$\int_{\Omega_e} w\left[u\frac{\partial C}{\partial x} + v\frac{\partial C}{\partial y} - D_s\left(\frac{\partial^2 C}{\partial x^2} + \frac{\partial^2 C}{\partial y^2}\right)\right]dxdy$$
$$= \int_{\Omega_e}\left[uw\frac{\partial C}{\partial x} + vw\frac{\partial C}{\partial y} + D_s\left(\frac{\partial w}{\partial x}\frac{\partial C}{\partial x} + \frac{\partial w}{\partial y}\frac{\partial C}{\partial y}\right)\right]dxdy - \oint_{\Gamma_e}\left(D_s w\frac{\partial C}{\partial x}n_x + D_s w\frac{\partial C}{\partial y}n_y\right)ds = 0 \tag{A.1}$$

where Ω_e is the domain a typical element, while Γ_e is the element boundary. The contour integral arising from this integration procedure provides the natural boundary conditions of our system in regard to diffusive fluxes. The integration of Eq. (A.1) utilized the divergence theorem as

$$-\int_{\Omega_e} D_s w(\nabla^2 C)dxdy = \int_{\Omega_e} D_s \nabla w\cdot\nabla C dxdy - \oint_{\Gamma_e} D_s w\nabla C\cdot\mathbf{n}ds \tag{A.2}$$

where,

$$\nabla\cdot\mathbf{n} = n_x\frac{\partial}{\partial x} + n_y\frac{\partial}{\partial y} \tag{A.3}$$

For the contour integral, define

$$q_n = D_s\nabla C\cdot\mathbf{n} = D_s\left(n_x\frac{\partial C}{\partial x} + n_y\frac{\partial C}{\partial y}\right) \tag{A.4}$$

where q_n is the prescribed diffusive flux of the solute, and (n_x, n_y) are the direction cosines of the outward pointing normal to Γ_e. As mentioned in [30], for the contour integral, it is not necessary to compute such integrals when a portion of Γ_e does not coincide with the boundary Γ of the total domain Ω. When the diffusive flux through the boundary is non-zero (and unknown), one has a diffusive permeable boundary, otherwise Neumann boundary conditions ($q_n = 0$) can be imposed properly on the impermeable boundaries [44]. For the permeable boundary at the membrane wall, Darcy's law can be applied [22], as

$$D_s\left(n_x\frac{\partial C}{\partial x} + n_y\frac{\partial C}{\partial y}\right) = D_s\frac{\partial C}{\partial n} = v_n(C - C_p) \tag{A.5}$$

in which v_n is the permeate velocity normal to membrane wall. Eq. (A.1) becomes

$$\int_{\Omega_e}\left[uw\frac{\partial C}{\partial x} + vw\frac{\partial C}{\partial y} + D_s\left(\frac{\partial w}{\partial x}\frac{\partial C}{\partial x} + \frac{\partial w}{\partial y}\frac{\partial C}{\partial y}\right)\right]dxdy - \oint_{\Gamma_e} v_n wCds = -\oint_{\Gamma_e} v_n wC_p ds \tag{A.6}$$

Galerkin's method was used for the weighted residual integral Eq. (A.1) by selecting the weight functions $w_i = \psi_i$ to be the same as the shape functions ψ_i in Eq. (15). Also, the shape functions ψ_i were selected to be Lagrange interpolation functions so that the approximate solution $C = \sum_{i=1}^{n} c_i^e\psi_i^e(x,y)$ is: 1) continuous over the element; 2) a complete polynomial, 3) and an interpolant of the primary variables between the nodes (c_i^e). For triangular elements the Lagrange interpolation functions can be calculated as [30]:

$$\psi_i^e = \frac{1}{2A_e}(\alpha_i^e + \beta_i^e x + \gamma_i^e y) \quad (i = 1,2,3) \tag{A.7}$$

in which the coefficients of the interpolation functions are:

$$\begin{cases}\alpha_i = x_j y_k - x_k y_j \\ \beta_i = y_j - y_k \\ \gamma_i = -(x_j - x_k)\end{cases} \quad (i \neq j \neq k; i,j \text{ and } k \text{ permute in a natual order}) \tag{A.8}$$

and A_e in Eq. (A.7) is the area of the element, $A_e = \alpha_1 + \alpha_2 + \alpha_3$.

Substitute weight functions w and approximate solution C into Eq. (A.6),

$$\int_{\Omega_e}\left[u\psi_i^e\sum_{j=1}^{n} c_j^e\frac{\partial\psi_j^e}{\partial x} + v\psi_i^e\sum_{j=1}^{n} c_j^e\frac{\partial\psi_j^e}{\partial y} + D_s\left(\frac{\partial\psi_i^e}{\partial x}\sum_{j=1}^{n} c_j^e\frac{\partial\psi_j^e}{\partial x} + \frac{\partial\psi_i^e}{\partial y}\sum_{j=1}^{n} c_j^e\frac{\partial\psi_j^e}{\partial y}\right)\right]dxdy$$
$$-\oint_{\Gamma_e} v_n\psi_i^e\sum_{j=1}^{n} c_j^e\psi_j^e ds = -\oint_{\Gamma_e} v_n\psi_i^e C_p ds \tag{A.9}$$

After integration, the weighted residual form can be discretized as,

$$\sum_{j=1}^{n} (K_{ij}^e + H_{ij}^e) c_j^e = Q_i^e \tag{A.10}$$

where matrix $[K_{ij}^e]$, $[H_{ij}^e]$ and vector $\{Q_i^e\}$ are finally obtained:

$$K_{ij}^e = \int_{\Omega_e} \left[u\psi_i^e \frac{\partial \psi_j^e}{\partial x} + v\psi_i^e \frac{\partial \psi_j^e}{\partial y} + D_s \left(\frac{\partial \psi_i^e}{\partial x}\frac{\partial \psi_j^e}{\partial x} + \frac{\partial \psi_i^e}{\partial y}\frac{\partial \psi_j^e}{\partial y} \right) \right] dxdy = \frac{\beta_j u^e}{6} + \frac{\gamma_j v^e}{6} + D_s \left(\frac{\beta_i \beta_j}{4A_e} + \frac{\gamma_i \gamma_j}{4A_e} \right) \tag{A.11}$$

$$H_{ij}^e = -\int_{\Gamma_e} v_n \psi_i^e \psi_j^e ds = -\left(\frac{v_{12n} h_{12}^e}{6} \begin{bmatrix} 2 & 1 & 0 \\ 1 & 2 & 0 \\ 0 & 0 & 0 \end{bmatrix} + \frac{v_{23n} h_{23}^e}{6} \begin{bmatrix} 0 & 0 & 0 \\ 0 & 2 & 1 \\ 0 & 1 & 2 \end{bmatrix} + \frac{v_{13n} h_{13}^e}{6} \begin{bmatrix} 2 & 0 & 1 \\ 0 & 0 & 0 \\ 1 & 0 & 2 \end{bmatrix} \right) \tag{A.12}$$

$$Q_i^e = -\oint_{\Gamma_e} v_n \psi_i^e C_p ds = -\frac{1}{2} C_p \begin{pmatrix} v_{12n} h_{12}^e + v_{31n} h_{31}^e \\ v_{12n} h_{12}^e + v_{23n} h_{23}^e \\ v_{31n} h_{31}^e + v_{23n} h_{23}^e \end{pmatrix} \tag{A.13}$$

In the matrix $[K_{ij}^e]$, u^e and v^e are average velocities of the three nodes in an element (labeled e), β and γ are the coefficients of the interpolation function for the element e, and A_e is the area of the element e. In $[H_{ij}^e]$ and $\{Q_i^e\}$, v_{12n}, v_{23n}, v_{31n} are the velocity normal to the boundaries of the triangular element, while h^e is the length of an element boundary.

References

[1] S. Sethi, G. Wetterau, Desalination of Seawater: Manual of Water Supply Practices, first ed., (2011).
[2] I.G. Wenten, Khoiruddin, Reverse osmosis applications: prospect and challenges, Desalination 391 (2016) 112–125, http://dx.doi.org/10.1016/j.desal.2015.12.011.
[3] C.Y. Tang, T.H. Chong, A.G. Fane, Colloidal interactions and fouling of NF and RO membranes: a review, Adv. Colloid Interf. Sci. 164 (2011) 126–143, http://dx.doi.org/10.1016/j.cis.2010.10.007.
[4] E.M.V. Hoek, J. Allred, T. Knoell, B.-H. Jeong, Modeling the effects of fouling on full-scale reverse osmosis processes, J. Membr. Sci. 314 (2008) 33–49, http://dx.doi.org/10.1016/j.memsci.2008.01.025.
[5] S.G. Yiantsios, D. Sioutopoulos, A.J. Karabelas, Colloidal fouling of RO membranes: an overview of key issues and efforts to develop improved prediction techniques, Desalination 183 (2005) 257–272, http://dx.doi.org/10.1016/j.desal.2005.02.052.
[6] A. Antony, J.H. Low, S. Gray, A.E. Childress, P. Le-Clech, G. Leslie, Scale formation and control in high pressure membrane water treatment systems: a review, J. Membr. Sci. 383 (2011) 1–16, http://dx.doi.org/10.1016/j.memsci.2011.08.054.
[7] S. Shirazi, C.J. Lin, D. Chen, Inorganic fouling of pressure-driven membrane processes - a critical review, Desalination 250 (2010) 236–248, http://dx.doi.org/10.1016/j.desal.2009.02.056.
[8] S.K. Gupta, T.R.D. Patel, R.C. Ackerberg, Wall heat/mass transfer in pulsatile flow, Chem. Eng. Sci. 37 (1982) 1727–1739, http://dx.doi.org/10.1016/0009-2509(82)80045-6.
[9] E.M.V. Hoek, M. Elimelech, Cake-enhanced concentration polarization: a new fouling mechanism for salt-rejecting membranes, Environ. Sci. Technol. 37 (2003) 5581–5588, http://dx.doi.org/10.1021/es0262636.
[10] T.J. Kennedy, R.L. Merson, B.J. McCoy, Improving permeation flux by pulsed reverse osmosis, Chem. Eng. Sci. 29 (1974) 1927–1931, http://dx.doi.org/10.1016/0009-2509(74)85010-4.
[11] D.E. Hadzismajlovic, C.D. Bertram, Flux enhancement in turbulent crossflow microfiltration of yeast using a collapsible-tube pulsation generator, J. Membr. Sci. 163 (1999) 123–134, http://dx.doi.org/10.1016/S0376-7388(99)00161-1.
[12] L. Malaeb, G.M. Ayoub, Reverse osmosis technology for water treatment: state of the art review, Desalination 267 (2011) 1–8, http://dx.doi.org/10.1016/j.desal.2010.09.001.
[13] W. Shi, M.M. Benjamin, Membrane interactions with NOM and an adsorbent in a vibratory shear enhanced filtration process (VSEP) system, J. Membr. Sci. 331 (2009) 11–20, http://dx.doi.org/10.1016/j.memsci.2008.12.027.
[14] W. Shi, M.M. Benjamin, Fouling of RO membranes in a vibratory shear enhanced filtration process (VSEP) system, J. Membr. Sci. 331 (2009) 11–20, http://dx.doi.org/10.1016/j.memsci.2008.12.027.
[15] W. Shi, M.M. Benjamin, Effect of shear rate on fouling in a Vibratory Shear Enhanced Processing (VSEP) RO system, J. Membr. Sci. 366 (2011) 148–157, http://dx.doi.org/10.1016/j.memsci.2010.09.051.
[16] R. Bian, K. Yamamoto, Y. Watanabe, The effect of shear rate on controlling the concentration polarization and membrane fouling, Desalination 131 (2000) 225–236.
[17] S. Lee, R.M. Lueptow, Control of scale formation in reverse osmosis by membrane rotation, Desalination 155 (2003) 131–139, http://dx.doi.org/10.1016/S0011-9164(03)00290-X.
[18] M. Mulder, Basic Principles of Membrane Technology, second ed., Kluwer Academic Publishers, 1996.
[19] M.C. Porter, Concentration polarization with membrane ultrafiltration, Ind. Eng. Chem. Prod. Res. Dev. 11 (1972) 234–248.
[20] J. Wang, D.S. Dlamini, A.K. Mishra, M.T.M. Pendergast, M.C.Y. Wong, B.B. Mamba, et al., A critical review of transport through osmotic membranes, J. Membr. Sci. 454 (2014) 516–537, http://dx.doi.org/10.1016/j.memsci.2013.12.034.
[21] I. Sutzkover, D. Hasson, R. Semiat, Simple technique for measuring the concentration polarization level in a reverse osmosis system, Desalination 131 (2000) 117–127, http://dx.doi.org/10.1016/S0011-9164(00)90012-2.
[22] S. Ma, L. Song, S.L. Ong, W.J. Ng, A 2-D streamline upwind Petrov/Galerkin finite element model for concentration polarization in spiral wound reverse osmosis modules, J. Membr. Sci. 244 (2004) 129–139, http://dx.doi.org/10.1016/j.memsci.2004.06.048.
[23] D.F. Fletcher, D.E. Wiley, A computational fluids dynamics study of buoyancy effects in reverse osmosis, J. Membr. Sci. 245 (2004) 175–181, http://dx.doi.org/10.1016/j.memsci.2004.07.023.
[24] V. Geraldes, V. Semião, M.N. Pinho, Numerical modelling of mass transfer in slits with semi-permeable membrane walls, Eng. Comput. 17 (2000) 192–218, http://dx.doi.org/10.1108/02644400010324857.
[25] A.S. Berman, Laminar flow in channels with porous walls, J. Appl. Phys. 24 (1953) 1232–1235, http://dx.doi.org/10.1063/1.1721476.
[26] Y. Moussy, A.D. Snider, Laminar flow over pipes with injection and suction through the porous wall at low Reynolds number, J. Membr. Sci. 327 (2009) 104–107, http://dx.doi.org/10.1016/j.memsci.2008.11.018.
[27] D. Bhattacharyya, S.L. Black, R.I. Kermode, Prediction of concentration polarization and flux behavior in reverse osmosis by numerical analysis, J. Membr. Sci. 48 (1990) 231–262, http://dx.doi.org/10.1016/0376-7388(90)85007-8.
[28] W.W. Focke, P.G.J.M. Nuijens, Velocity profile caused by a high porosity spacer between parallel plates (membranes), Desalination 49 (1984) 243–253, http://dx.doi.org/10.1016/0011-9164(84)85036-5.
[29] M. Shakaib, S.M.F. Hasani, M. Mahmood, Study on the effects of spacer geometry in membrane feed channels using three-dimensional computational flow modeling, J. Membr. Sci. 297 (2007) 74–89, http://dx.doi.org/10.1016/j.memsci.2007.03.010.
[30] J.N. Reddy, An Introduction to the Finite Element Method, third ed., McGraw-Hill, 2006.
[31] V. Nassehi, Practical Aspects of Finite Element Modelling of Polymer Processing, first ed., John Wiley & Sons, Ltd., 2002.
[32] C.J. Richardson, V. Nassehi, Finite element modelling of concentration profiles in flow domains with curved porous boundaries, Chem. Eng. Sci. 58 (2003) 2491–2503, http://dx.doi.org/10.1016/S0009-2509(03)00118-0.
[33] A. Rahardianto, W.Y. Shih, R.W. Lee, Y. Cohen, Diagnostic characterization of gypsum scale formation and control in RO membrane desalination of brackish water, J. Membr. Sci. 279 (2006) 655–668, http://dx.doi.org/10.1016/j.memsci.2005.12.059.
[34] D. Rana, T. Matsuura, Surface modifications for antifouling membranes, Chem. Rev. 110 (2010) 2448–2471, http://dx.doi.org/10.1021/cr800208y.
[35] W.Y. Shih, A. Rahardianto, R.W. Lee, Y. Cohen, Morphometric characterization of calcium sulfate dihydrate (gypsum) scale on reverse osmosis membranes, J. Membr. Sci. 252 (2005) 253–263, http://dx.doi.org/10.1016/j.memsci.2004.12.023.
[36] E.W. Tow, J.H. Lienhard V, Quantifying osmotic membrane fouling to enable comparisons across diverse processes, J. Membr. Sci. 511 (2016) 92–107, http://dx.doi.org/10.1016/j.memsci.2016.03.040.
[37] M.A. Javeed, K. Chinu, H.K. Shon, S. Vigneswaran, Effect of pre-treatment on fouling propensity of feed as depicted by the modified fouling index (MFI) and cross-flow sampler-modified fouling index (CFS-MFI), Desalination 238 (2009) 98–108, http://dx.doi.org/10.1016/j.desal.2008.01.040.
[38] J.C. Schippers, J. Verdouw, The modified fouling index, a method of determing the fouling characteristics of water, Desalination 32 (1980) 137–148, http://dx.doi.org/10.1016/S0011-9164(00)86014-2.
[39] K. Katsoufidou, S.G. Yiantsios, A.J. Karabelas, Experimental study of ultrafiltration membrane fouling by sodium alginate and flux recovery by backwashing, J. Membr. Sci. 300 (2007) 137–146, http://dx.doi.org/10.1016/j.memsci.2007.05.017.
[40] K.Y. Jee, D.H. Shin, Y.T. Lee, Surface modification of polyamide RO membrane for improved fouling resistance, Desalination 394 (2016) 131–137, http://dx.doi.org/10.1016/j.desal.2016.05.013.
[41] T.D. Wolfe, Membrane Process Optimization Technology, (2003).
[42] A. Alhadidi, A.J.B. Kemperman, B. Blankert, J.C. Schippers, M. Wessling,

W.G.J. van der Meer, Silt density index and modified fouling index relation, and effect of pressure, temperature and membrane resistance, Desalination 273 (2011) 48–56, http://dx.doi.org/10.1016/j.desal.2010.11.031.

[43] E. Brauns, E. Van Hoof, B. Molenberghs, C. Dotremont, W. Doyen, R. Leysen, A new method of measuring and presenting the membrane fouling potential, Desalination 150 (2002) 31–43, http://dx.doi.org/10.1016/S0011-9164(02)00927-X.

[44] F. Padilla, Y. Secretan, M. Leclerc, On open boundaries in the finite element approximation of two-dimensional advection-diffusion flows, Int. J. Numer. Methods Eng. 2516 (1997) 2493–2516.